# Electron Transport Dynamics in Redox-Molecule-Terminated Branched Oligomer Wires on Au(111)

Ryota Sakamoto,[†] Shunsuke Katagiri,[†] Hiroaki Maeda,[†] Yoshihiko Nishimori,[†] Seiji Miyashita,[‡] and Hiroshi Nishihara*,[†]

[†]Department of Chemistry, Graduate School of Science, The University of Tokyo, 7-3-1 Hongo, Bunkyo-ku, Tokyo 113-0033, Japan
[‡]Department of Physics, Graduate School of Science, The University of Tokyo, 7-3-1 Hongo, Bunkyo-ku, Tokyo 113-0033, Japan

S *Supporting Information*
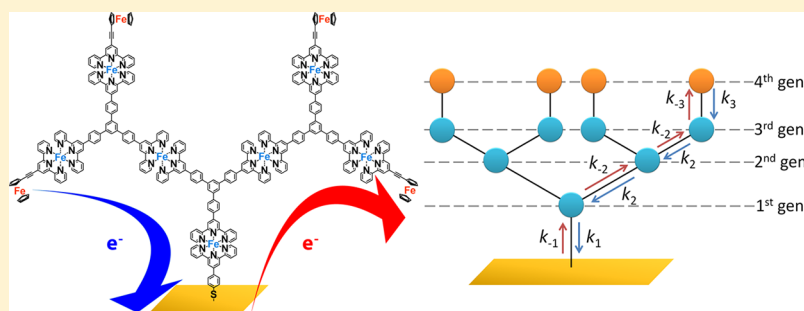
ABSTRACT: Dendritic bis(terpyridine)iron(II) wires with terminal ferrocene units were synthesized on a Au(111) surface by stepwise coordination using a three-way terpyridine ligand, a ferrocene-modified terpyridine ligand, and Fe(II) ions. Potential–step chronoamperometry, which applied overpotentials to induce the redox of the terminal ferrocene, revealed an unusual electron-transport phenomenon. The current–time profile did not follow an exponential decay that is common for linear molecular wire systems. The nonexponentiality was more prominent in the forward electron-transport direction (from the terminal ferrocene to the gold electrode, oxidation) than in the reverse direction (from the gold electrode to the terminal ferrocenium, reduction). A plateau and a steep fall were observed in the former. We propose a simple electron transport mechanism based on intrawire electron hopping between two adjacent redox-active sites, and the numerical simulation thereof reproduced the series of "asymmetric" potential–step chronoamperometry results for both linear and branched bis(terpyridine)iron(II) wires.

INTRODUCTION

Since the introduction of conceptual proposals of molecular electronic devices from the 1970s to the 1980s,[1−5] research toward molecular electronics has been developed and expanded significantly. A principal area of interest is the way in which electrons pass through molecular arrays such as electrical wirings. Electrodes with surface-immobilized molecular wires operate as molecule-based devices (e.g., memories, logic gates, and switches).[6−8] The modified electrode may also be a convenient platform for evaluating the ability of molecular wires to transport electrons. This evaluation may be conducted by measuring the faradaic current of the redox active species immobilized at the tip of the molecular wire.[9,10] This type of experiment is simple and easy to conduct, but its experimental outcomes are often associated with the electrical conductivity of the molecular wire using elaborate and difficult molecular junction techniques.[11−13]

We are interested in how electrons travel through "branched" molecular wires, as this knowledge would be useful in understanding molecular parallel circuits[14] and splitters.[15] Branched molecular wires are rarely precisely fabricated.[16,17] We have reported previously on the synthesis of bis-

(terpyridine)metal complex $[M(tpy)_2$, tpy = 2,2′:6′,2″-terpyridine, M = Fe and/or Co] oligomer wires on electrode surfaces (Figure 1).[18,19] The molecular wire is fabricated by stepwise coordination, where there is alternating complexation between terpyridine ligands (e.g., A_H, L_L, and T in Figure 1) and metal ions. A programmable method allows the *in situ* construction of molecular wires with desired compositions, lengths, and structures. Furthermore, not only commonplace linear wires but also dendritic wires may be fabricated,[20,21] which is an important feature for the present work. We have demonstrated that intrawire redox conduction for the $M(tpy)_2$ units occurs along the molecular wires.[20] We have also investigated the ability of linear $M(tpy)_2$ wires modified with a terminal redox site (e.g., $Au-[A_H(FeL_L)_nFeT]$ equipped with terminal ferrocene in Figure 1) to transport electrons over a long range. The wires possess small distance decay constants ($\beta^d =$ 0.002 Å^{-1} and 0.02 Å^{-1} for the Co and Fe centers, respectively).[22−25]
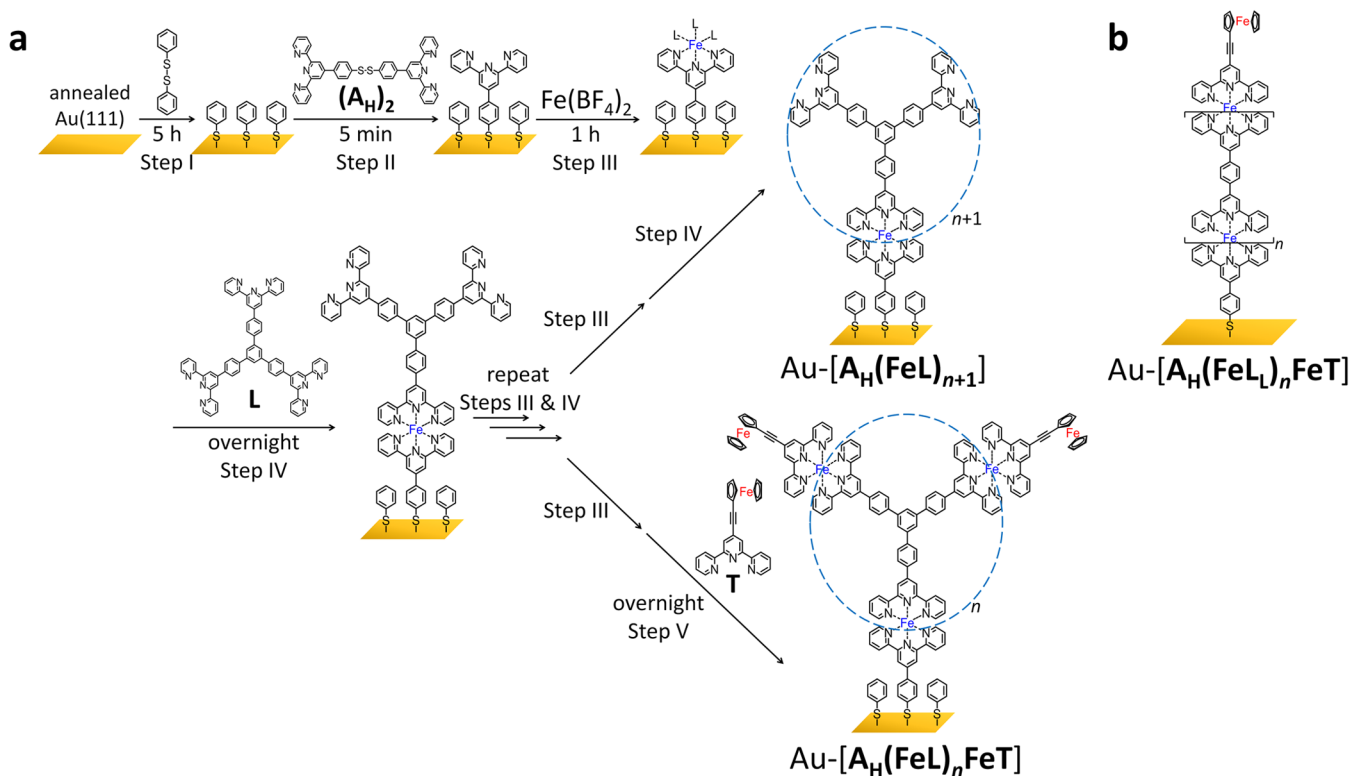
Figure 1. Linear and branched Fe(tpy)₂ oligomer wires. (a) Stepwise coordination procedure for the preparation of Au−[$A_H(FeL)_nFeT$] and Au−[$A_H(FeL)_{n+1}$]. Step I: phenyl disulfide in chloroform; Step II: anchor ligand (A_H)₂ in chloroform; Step III: Fe(BF₄)₂ in ethanol; Step IV: trident bridging ligand **L** in chloroform; and Step V: terminal ligand **T** in chloroform. (b) Chemical structure of linear Fe(tpy)₂ oligomer wire Au−[$A_H(FeL_L)_nFeT$].

In the present paper, we reveal a characteristic electron-transport phenomenon in branched Fe(tpy)₂ oligomer wires furnished with terminal ferrocene units (Au−[$A_H(FeL)_nFeT$], Figure 1). We determined and analyzed the faradaic current of the ferrocene unit by pontential−step chronoamperometry (PSCA). Note that the branched wire undergoes unusual electron transport, which is reflected in nonexponential and asymmetric faradaic current decays; i.e., there are different current profiles for the oxidation and reduction processes. The unusual chronoamperogram is reproduced closely by a simple but effective kinetic simulation based on an intrawire sequential electron-hopping mechanism.

RESULTS AND DISCUSSION

Preparation of Dendritic Fe(tpy)₂ Wires. A series of Au−[$A_H(FeL)_nFeT$] and Au−[$A_H(FeL)_{n+1}$] (n = 1−3) were fabricated by stepwise coordination as illustrated in Figure 1a (see also Figure S1 and Supporting Information for details). To suppress steric repulsion among adjacent dendritic wires, the anchor ligand A_H was implanted sparsely onto the Au(111) surface. A self-assembled monolayer of phenyl disulfide was prepared on a Au substrate (Step I), accompanied by immersion in a chloroform solution of disulfide (A_H)₂ for a short period (5 min, Step II, via thiol exchange reaction). The tpy-terminated Au substrate was then soaked in an Fe(BF₄)₂ solution to allow for complexation with Fe(II) ions (Step III). The Fe(tpy)₂ motif was completed in Step IV where the modified electrode was dipped overnight in a chloroform solution of three-way-bridging ligand **L**. Iteration of Steps III and IV resulted in an elongation of the dendritic wires; n + 1 repeats of these two steps lead to the formation of Au−

[$A_H(FeL)_{n+1}$]. When the last Step IV is replaced with Step V, which uses a chloroform solution of ferrocene-appended tpy ligand **T**, the molecular wire growth is terminated, and Au−[$A_H(FeL)_nFeT$] is generated.

Characterization of Dendritic Fe(tpy)₂ Wires. A representative scanning tunneling microscope (STM) image of Au−[$A_H(FeL)_2FeT$] is shown in Figure 2a, which features sparsely placed cylinder-like structures. The diameter of the top face of the cylinder is ∼5 nm, which is consistent with the size of the branched molecular wire.

X-ray photoelectron spectroscopy (XPS) measurements were also performed for Au−[$A_H(FeL)_2FeT$] (Figure 2b−e). Peaks derived from the constitutive elements, N 1s (binding energy: 400.2 eV), F 1s (685.6 eV), S 2p (161.0 eV), and Fe 2p (709.0 eV for $2p_{1/2}$; 721.4 eV for $2p_{3/2}$), are visible. Fluorine is present as the counteranion, BF₄⁻. The binding energies are typical of those for Fe(tpy)₂ oligomer wires reported previously,[21,25] which indicates that the molecular wire was formed successfully and was immobilized on the gold electrode through the intact Au−S bond (i.e., there was no oxidized sulfur such as disulfide). Cyclic voltammetry was conducted to determine the redox activity and the surface coverage of Au−[$A_H(FeL)_nFeT$]. The cyclic voltammograms (CVs) shown in Figure 3a exhibit two redox waves at 0.15 and 0.70 V vs ferrocenium/ferrocene, which can be assigned to the terminal ferrocene⁺/⁰ and [Fe(tpy)₂]³⁺/²⁺ redox couples, respectively. Geometrically, the ideal surface coverage of the Fe(tpy)₂ and ferrocene units is proportional to $2^{n+1} − 1$ and 2^n, respectively (dashed lines in Figure 3b). The experimental surface coverage increases in good agreement with the ideal coverage up to n = 2, whereas the surface coverage of Au−[$A_H(FeL)_3FeT$] does not follow
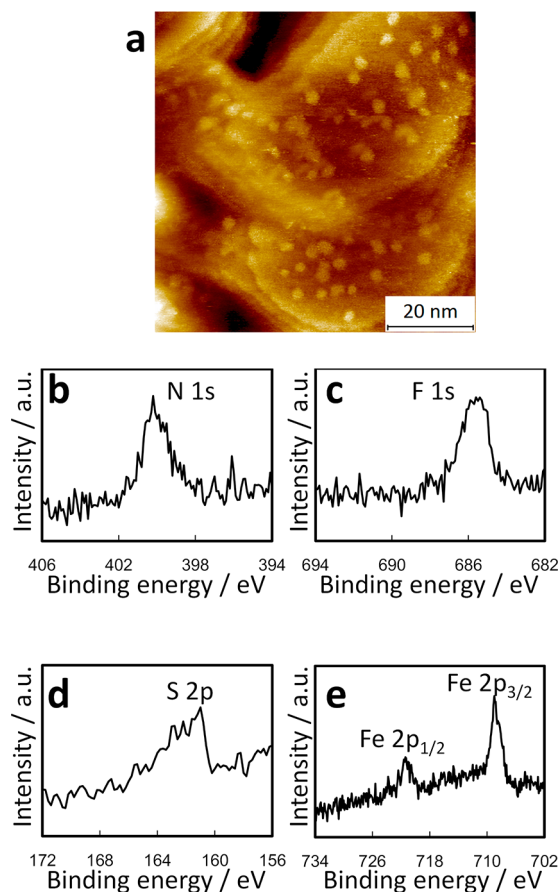
Figure 2. Characterization of Au−[A$_H$(FeL)$_n$FeT]. (a) Representative STM image of Au−[A$_H$(FeL)$_2$FeT] (75 nm × 75 nm). (b−e) XPS of Au−[A$_H$(FeL)$_2$FeT] focusing on each element: (b) N 1s, (c) F 1s, (d) S 2p, and (e) Fe 2p.

Figure 3. Electrochemical characterization of Au−[A$_H$(FeL)$_n$FeT]. (a) Cyclic voltammograms (CVs) of Au−[A$_H$(FeL)$_n$FeT] (n = 1−3) at a scan rate of 100 mV s^{-1}. (b) Ideal and experimental surface coverages (in mol cm^{-2}) of [Fe(tpy)$_2$] (blue) and ferrocene (red) units. Dashed lines express the ideal surface coverages for [Fe(tpy)$_2$] (proportional to 2^{n+1} − 1) and ferrocene (2^n) units. The plot at n = 0 is derived from Au−[A$_H$(FeL)]. (c−e) (left) CVs at various scan rates (25−500 mV s^{-1}), and (right) plots for peak currents vs scan rates for [Fe(tpy)$_2$] (blue) and ferrocene (red) units: (c) n = 1, (d) n = 2, and (e) n = 3. All CVs were measured in 1 M Bu$_4$ClO$_4$−dichloromethane.

the theoretical value (plots in Figure 3b). Similarly, the successful formation of Au−[A$_H$(FeL)$_{n+1}$] is confirmed up to n = 2 by ideal growth of the surface coverage of the Fe(tpy)$_2$ unit (Figure S2). Steric interference is presumed between the terminus of the dendritic wire and electrode surface when n reaches 3.

We also surveyed the scan−rate dependence of CVs for Au−[A$_H$(FeL)$_n$FeT] to gain insight into the electron transfer rate between the ferrocene moiety and the gold electrode. The [Fe(tpy)$_2$]$^{3+/2+}$ redox couple exhibits nernstian behavior for electrode-bound species. The redox wave is reversible for scan rates up to 500 mV s^{-1}, and there is a linear relationship between the peak current and the scan rate (Figure 3c−e). In contrast, the redox behavior of the terminal ferrocene depends on n. It undergoes a nernstian redox reaction in Au−[A$_H$(FeL)$_1$FeT] (Figure 3c), whereas a slight peak separation is found in Au−[A$_H$(FeL)$_2$FeT] (Figure 3d). The peak separation increases in Au−[A$_H$(FeL)$_3$FeT]. Another anodic peak appears at approximately 0.35 V, which is ascribed to charge trapping (Figure 3e).[26−28] These observations indicate that the electron transfer between the ferrocenyl group and gold electrode occurs in a through-bond fashion: If the through-space or direct contact electron transfer mechanism were vaild, Au−[A$_H$(FeL)$_3$FeT], which might possess shorter distances between the ferrocene sites and Au(111) surface than Au−[A$_H$(FeL)FeT] and Au−[A$_H$(FeL)$_2$FeT] because of the characteristic dendritic structure, would have a narrower peak
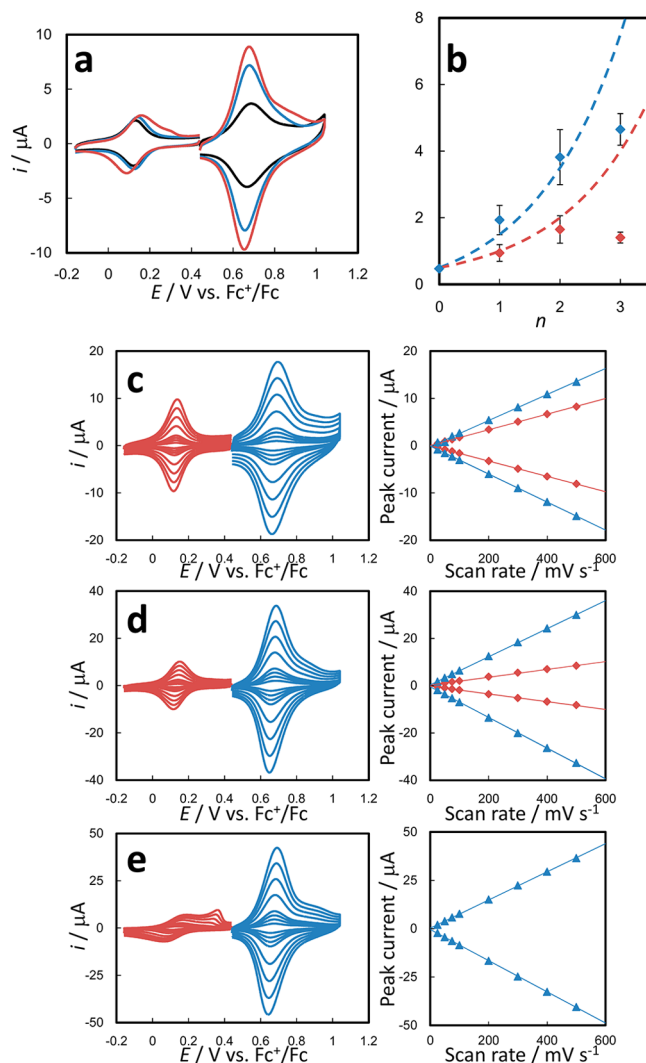
separation (i.e., more rapid electron transfer). Therefore, the branched Fe(tpy)$_2$ oligomer wire may mediate electron transfer between the terminal ferrocene and gold electrode effectively, but still acts as "resistance", which leads to the dependence on n as discussed above. The deceleration in electron transport, however, allows us to extract kinetic information by using electrochemical techniques.

Electron Transport and Its Mechanism in Dendritic Fe(tpy)$_2$ Wires. Figure 4b,c,e,f,h,i displays the PSCA results for the oxidation and reduction of the terminal ferrocene in Au−[A$_H$(FeL)$_n$FeT] at +0.35 and −0.35 V overpotentials. A distinctive feature of the PSCA profile (i_{exp}−t plot) lies in asymmetric electron transport. The deviation from the exponential decay is more substantial in the oxidation process, which shows an unusual plateau-like region. The asymmetry in the electron transport is more conspicuous as n increases. This
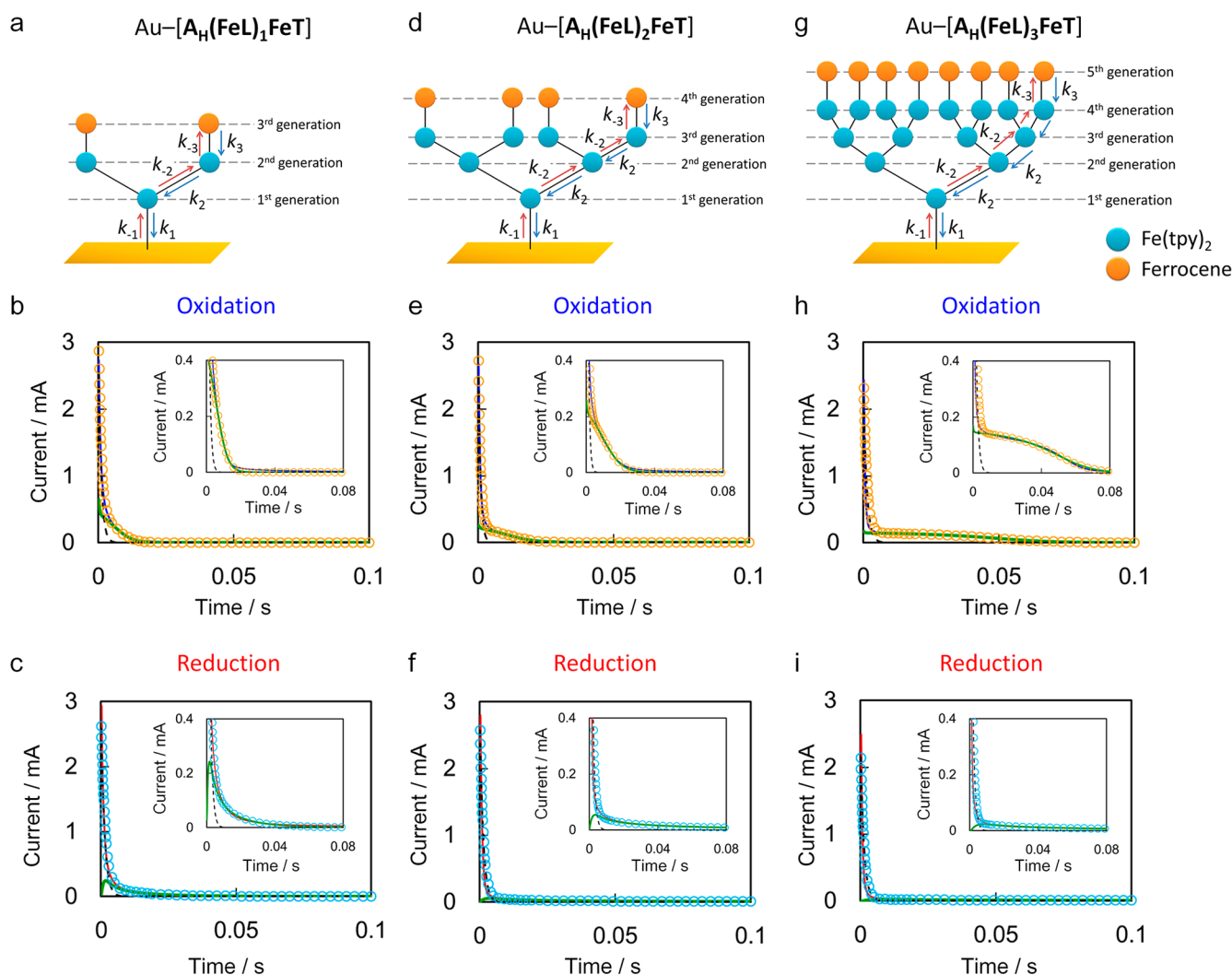
Figure 4. Electron transport through $Fe(tpy)_2$ branched oligomer wires. (a,d,g) Electron transport models for: (a) Au−[$A_H(FeL)_1FeT$]; (d) Au−[$A_H(FeL)_2FeT$]; (g) Au−[$A_H(FeL)_3FeT$]. (b,c,e,f,h,i) Representative experimental (i_{exp}−t) and simulated (i_{sim}−t) current−time plots for (b,c) Au−[$A_H(FeL)_1FeT$], (e,f) Au−[$A_H(FeL)_2FeT$], and (h,i) Au−[$A_H(FeL)_3FeT$]. Legend. Blue solid line: i_{exp} for oxidation with an overpotential of +0.35 V for the ferrocene moiety; red solid line: i_{exp} for reduction with −0.35 V; black dashed line: electric double layer charging current i_{DL}; green solid line: faradaic current i_F; orange circles; i_{sim} for the oxidation; light-blue circles: i_{sim} for the reduction. See Tables S1−S3 for the parameters used in the simulation.

series of current−decay features is different from those of previously reported linear molecular wire systems furnished with redox-active termini.[9,29,30]

To elucidate the unique electron transport in Au−[$A_H(FeL)_nFeT$], a simplified but effective electron transport mechanism was considered and numerically simulated. Figure 4a,d,g illustrates the mechanism, which allows the traveling electrons to occupy the redox-active hopping sites (i.e., the terminal ferrocene and $Fe(tpy)_2$ units) and the gold electrode. They hop between neighboring sites exclusively and never undergo inter-wire hopping. The hopping site can be either electron-filled (ferrocene⁰ and $[Fe(tpy)_2]^{2+}$) or electron-deficient (ferrocene•⁺ and $[Fe(tpy)_2]^{3+}$). The electrode serves as an electron reservoir, such that it may accept or provide an infinite number of electrons. The hopping process may be classified into three steps. The first step is that between the gold electrode and the first-generation $Fe(tpy)_2$ unit. The rate constants for electron injection from the $Fe(tpy)_2$ to the electrode and *vice versa* are denoted as k_1 and k_{-1}, respectively. Another process is electron exchange between adjacent

$Fe(tpy)_2$ units. The second-order electron self-exchange rate constants are k_2 and k_{-2}. The last process is electron hopping between the terminal ferrocene and neighboring $Fe(tpy)_2$ unit, with rate constants k_3 and k_{-3}. In this scheme, a generalized set of kinetic equations in Au−[$A_H(FeL)_nFeT$] is expressed as follows:

$$dP_1/dt = 2[k_2P_2(1 - P_1) - k_{-2}P_1(1 - P_2)] - k_1P_1$$
$$+ k_{-1}(1 - P_1) \tag{1a}$$

$$dP_k/dt = 2[k_2P_{k+1}(1 - P_k) - k_{-2}P_k(1 - P_{k+1})]$$
$$- k_2P_k(1 - P_{k-1})$$
$$+ k_{-2}P_{k-1}(1 - P_k) \quad (k = 2, 3, ..., n) \tag{1b}$$

$$dP_{n+1}/dt = k_3P_{n+2}(1 - P_{n+1}) - k_{-3}P_{n+1}(1 - P_{n+2})$$
$$- k_2P_{n+1}(1 - P_n) + k_{-2}P_n(1 - P_{n+1}) \tag{1c}$$

Table 1. Average Electron Transfer Rate Constants k_l ($l = \pm1, \pm2, \pm3$) Extracted from the Simulation for Branched Au−[$A_H(FeL)_nFeT$] ($n = 1-3$) and Linear Au−[$A_H(FeL_L)_nFeT$] ($n = 1, 2$)

		k_1/s^{-1}	k_{-1}/s^{-1}	$k_2, k_{-2}/s^{-1}$	k_3/s^{-1}	k_{-3}/s^{-1}
Au−[$A_H(FeL)_1FeT$]	oxidation	330 ± 29	4400 ± 380	17700 ± 150	4200 ± 950	70 ± 45
	reduction	11 ± 18	1900 ± 330	17700 ± 150	4200 ± 950	130 ± 110
Au−[$A_H(FeL)_2FeT$]	oxidation	226 ± 74	3400 ± 250	17100 ± 190	4600 ± 1200	56 ± 66
	reduction	0.001 ± 0.001	4000 ± 650	17100 ± 190	4600 ± 1200	64 ± 55
Au−[$A_H(FeL)_3FeT$]	oxidation	170 ± 30	4100 ± 760	18200 ± 320	5800 ± 550	31 ± 12
	reduction	5 ± 5	3000 ± 1800	18200 ± 320	5800 ± 550	13 ± 7
Au−[$A_H(FeL_L)_1FeT$]	oxidation	250 ± 62	3700 ± 500	17300 ± 520	4300 ± 1100	14 ± 16
	reduction	10 ± 9	1600 ± 440	17300 ± 520	4300 ± 1100	100 ± 35
Au−[$A_H(FeL_L)_2FeT$]	oxidation	200 ± 39	4900 ± 620	16700 ± 450	4700 ± 870	16 ± 17
	reduction	3 ± 3	1700 ± 210	16700 ± 450	4700 ± 870	100 ± 32

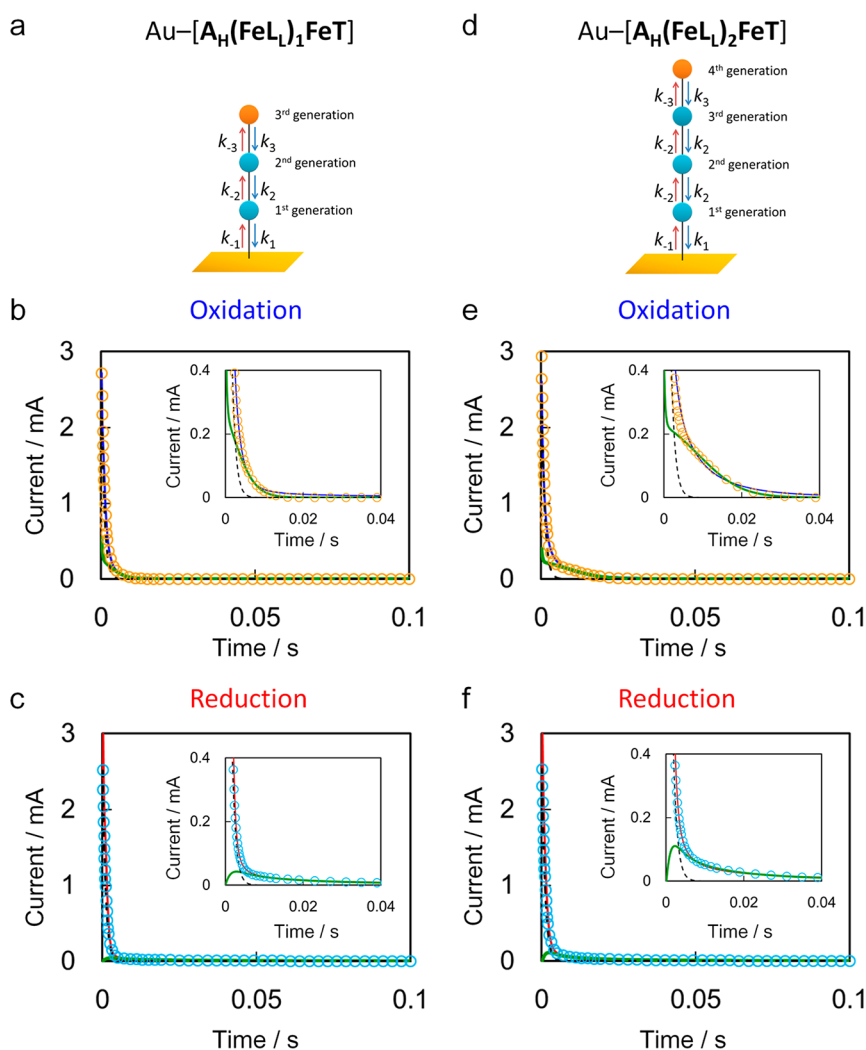**Figure 5.** Electron transport through Fe(tpy)₂ linear oligomer wires. (a,d) Electron transport models for: (a) Au−[$A_H(FeL_L)_1FeT$]; (d) Au−[$A_H(FeL_L)_2FeT$]. (b,c,e,f) Representative experimental ($i_{exp}-t$) and simulated ($i_{sim}-t$) current−time plots for: (b,c) Au−[$A_H(FeL_L)_1FeT$], (e,f) Au−[$A_H(FeL_L)_2FeT$]. Legend. Blue solid line: i_{exp} for oxidation with an overpotential of +0.35 V for the ferrocene moiety; red solid line: i_{exp} for reduction with −0.35 V; black dashed line: electric double layer charging current i_{DL}; green solid line: faradaic current i_F; orange circles; i_{sim} for the oxidation; light-blue circles: i_{sim} for the reduction. See Tables S4 and S5 for the parameters used in the simulation.

$$dP_{n+2}/dt = -k_3 P_{n+2}(1 - P_{n+1}) + k_{-3} P_{n+1}(1 - P_{n+2})$$
(1d)

where P_m is the electron population ratio for the mth generation (see Figure 4a,d,g for the definition of the generation and the Experimental Section for each specific case). In this scheme, the

faradaic current i_F, which is derived from the terminal ferrocene unit, is expressed as follows:

$$i_F = FA\Gamma[k_1 P_1 - k_{-1}(1 - P_1)]$$
(2)

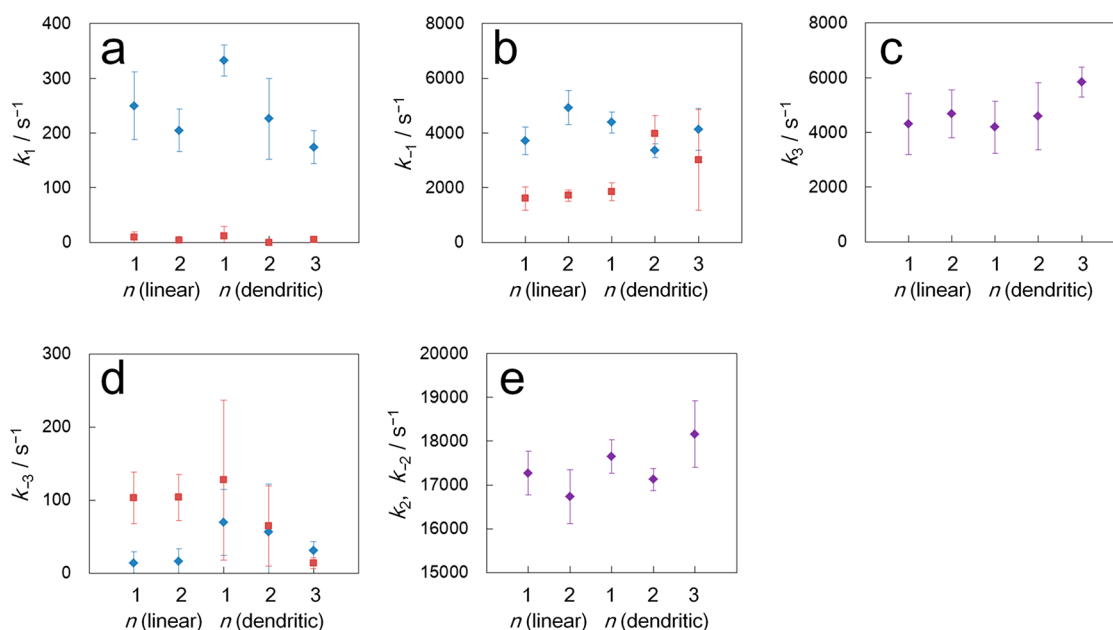where F, A, and Γ are the Faraday constant, the electrode area, and the surface coverage (in mol cm⁻²) of the dendritic wire,

Figure 6. Average electron transfer rate constants k_l ($l = \pm1, \pm2, \pm3$) extracted from the simulation for branched Au$-[\mathbf{A_H(FeL)_nFeT}]$ ($n = 1-3$) and linear Au$-[\mathbf{A_H(FeL_L)_nFeT}]$ ($n = 1, 2$). Blue and red plots exhibit the rate constants for oxidation and reduction, and purple ones for constrained parameters. (a) k_1, (b) k_{-1}, (c) k_3, (d) k_{-3}, and (e) k_2 and k_{-2}.

respectively. The simulated total current i_{sim} corresponds to the sum of i_F and the electric double layer charging current i_{DL} decaying in an exponential fashion, as follows:

$$i_{sim} = i_F + i_{DL} \tag{3}$$

where the term i_{DL} corresponds to a charging current to the electric double layer, which is dominated by experimentally measurable parameters, solution resistance R_{sol} and capacitance C_{DL}. Therefore, the numerical simulation is equivalent to the reproduction of i_{exp} with i_{sim}, while varying the k_l ($l = \pm1, \pm2, \pm3$) values. The resultant i_{sim} (as orange or light-blue circles) shows good consistency with the experimental current–time profile (Figure 4b,c,e,f,h,i). Figure 4b,c,e,f,h,i also contains i_{DL} (as black dashed line) and i_F (as green solid line), which shows that i_F is responsible for the peculiar plateau region for the oxidation process. Used parameters including the k values are summarized in Tables S1−S3. We note that three independent samples were subjected to the simulation for each branched wire, again showing good fitting (Figures S3−S5 and Tables S1−S3. Average k values collected from the three samples are assembled in Table 1 and Figure 6 and are discussed below.

To ensure the validity of the electron-transport model and simulation suggested here, electron transport through a linear wire Au$-[\mathbf{A_H(FeL_L)_nFeT}]^{22−25}$ ($n = 1$ and 2; Figure 5) was also analyzed. This investigation also allows us to exclude an electron transfer pathway based on the through-space or direct contact mechanism, because the linear wire is unlikely to experience a significant approach between the ferrocene site and gold electrode surface. By assuming that the set of electron-hopping processes is the same as for the branched wire, the generalized kinetic equations are represented as follows:

$$dP_1/dt = k_2P_2(1 - P_1) - k_{-2}P_1(1 - P_2)$$
$$- k_1P_1 + k_{-1}(1 - P_1) \tag{4a}$$

$$dP_k/dt = k_2P_{k+1}(1 - P_k) - k_{-2}P_k(1 - P_{k+1})$$
$$- k_2P_k(1 - P_{k-1}) + k_{-2}P_{k-1}(1 - P_k)$$
$$(k = 2, 3, ..., n) \tag{4b}$$

$$dP_{n+1}/dt = k_3P_{n+2}(1 - P_{n+1}) - k_{-3}P_{n+1}(1 - P_{n+2})$$
$$- k_2P_{n+1}(1 - P_n) + k_{-2}P_n(1 - P_{n+1}) \tag{4c}$$

$$dP_{n+2}/dt = -k_3P_{n+2}(1 - P_{n+1}) + k_{-3}P_{n+1}(1 - P_{n+2}) \tag{4d}$$

see the method section for each specific case. The faradaic current i_F and simulated total current i_{sim} may be obtained from eqs 2 and 3, respectively. The resultant $i_{sim}-t$ plots are overlain on the $i_{exp}-t$ plots (Figure 5b,c,f), and again show good consistency. We also applied the same simulation to two other independent samples, again reproducing the PSCA results (Figures S6 and S7; Tables S4 and S5).

Table 1 and Figure 6 summarize average electron transfer rate constants k_l ($l = \pm1, \pm2, \pm3$) obtained from the simulation for branched Au$-[\mathbf{A_H(FeL)_nFeT}]$ ($n = 1-3$) and linear Au$-[\mathbf{A_H(FeL_L)_nFeT}]$ ($n = 1, 2$). These data show that each parameter is converged within a certain range, considering its standard deviation, for both branched and linear wires. This result is reasonable, at least for $k_{\pm1}$ and $k_{\pm3}$ values, because the two wire systems adopt the same surface−anchor ($\mathbf{A_H}$) and terminal ($\mathbf{T}$) tpy ligands, which are responsible for, respectively, the $k_{\pm1}$ and $k_{\pm3}$ values.

■ CONCLUSIONS

Dendritic Fe(tpy)$_2$ oligomer wires with multiple terminal ferrocene units, Au$-[\mathbf{A_H(FeL)_nFeT}]$, were realized on a Au(111) electrode surface by stepwise coordination using components of trident terpyridine ligand $\mathbf{L}$, ferrocene-conjugated terpyridine ligand $\mathbf{T}$, and Fe(II) ions. Scanning tunneling microscopy, X-ray photoelectron spectroscopy, and electrochemical measurements confirmed that dendritic wires

up to $n = 2$ were fabricated successfully. Electron transport between the terminal ferrocene unit and the gold electrode through the dendritic wire was studied by PSCA, revealing asymmetric and nonexponential faradaic current decays. An electron transport mechanism based on intrawire electron hopping between two adjacent redox active sites was considered. Its numerical simulation reproduced the characteristic electron transport in the branched wire closely. The same simulation also accounts for the electron-transport phenomenon in linear $Fe(tpy)_2$ oligomer wire $Au-[A_H(FeL_L)_nFeT]$ which comprises similar components. The electron-hopping rate constants, $k_{\pm 1}$ (between the electrode and the $Fe(tpy)_2$ unit), $k_{\pm 2}$ (between two neighboring $Fe(tpy)_2$ units), and $k_{\pm 3}$ (between the $Fe(tpy)_2$ unit and the terminal ferrocene unit), which were extracted from the simulation series converged to similar values in the dendritic and linear wires. These results confirm the validity of the electron transport mechanism. In this work, we clarified for the first time the electron transport mechanism of a branched molecular wire system.

■ EXPERIMENTAL SECTION

Materials. $(A_H)_2$,[22] L,[31] and T[32] were synthesized according to the previous literatures. Natural mica plates were purchased from The Nilaco Corporation. Tetrabutylammonium perchlorate (Bu_4ClO_4, purchased from Tokyo Chemical Industry Co., Ltd.) was recrystallized from HPLC-grade ethanol and dried under vacuum for 24 h. HPLC-grade solvents (ethanol, chloroform, and dichloromethane) were purchased from Kanto Chemical Co., Inc., and used as received. $4',4''''$-(1,4-Phenylene)bis(2,2':6',2''-terpyridine) (L_L) and iron(II) tetrafluoroborate hexahydrate were purchased from Sigma–Aldrich. Water was purified by AUTOPURE WD500 (Yamato Scientific Co., Ltd.) and Simplicity UV (Millipore).

Electrochemical Measurements. Electrochemical measurements were conducted using a modified Au/mica plate (electrode area: 0.264 cm^2) as a working electrode, a helical Pt wire as a counter electrode, and a laboratory-made Ag^+/Ag (10 mM $AgClO_4$ in 0.1 M Bu_4ClO_4–MeCN) electrode as a reference electrode in a standard one-component cell at room temperature. Cyclic voltammetry and PSCA were implemented using an ALS 650DT electrochemical analyzer (BAS Inc.). All experiments were carried out in 1 M Bu_4ClO_4–dichloromethane, to ensure that the electron transfer rate is not limited by the movement of the counteranion (ClO_4^-).[20] The electrolyte solution was degassed by Ar bubbling, and ferrocene was used as an internal standard. In PSCA, the working electrode potential was first kept at $E^{0'} - \eta$ ($E^{0'}$ is the formal potential of the terminal ferrocene, 0.15 V vs Fc^+/Fc; η is the overpotential, +0.35 V in the present case), then a potential step to $E^{0'} + \eta$ was applied to acquire an oxidative amperogram. Finally, an electrode potential of $E^{0'} - \eta$ was applied again to obtain a reductive amperogram. At least three samples were prepared under the same conditions, and average values were obtained for the surface coverage and k_l values. The error bars in Figure 6 correspond to the standard deviation.

Scanning Probe Microscopy (SPM) Measurements. STM measurement was conducted using an Aglient 5500 instrument under ambient conditions. As a probe, a Pt–Ir alloy wire (4:1, diameter: 0.25 mm, purchased from The Nilaco Corporation) was used: It was cut off using a nipper to get a sharp edge prior to use.

X-ray Photoelectron Spectroscopy (XPS) Measurements. X-ray photoelectron spectra were measured using a PHI5000 VersaProbe (ULVAC–PHI) spectrometer. Monochromatic Al K_α (20 kV, 100 W) was used as an X-ray source. All spectra were calibrated according to the peak for Au(0) [$4f_{7/2}$ at 83.8 eV].

Numerical Simulation for PSCA. In order to reproduce the PSCAs observed in the branched and linear $Fe(tpy)_2$ oligomer wires, a sequential electron hopping model shown in Figures 4a,d,g and 5a,d was considered. In the case of $Au-[A_H(FeL)_1FeT]$, the series of kinetic equations for branched wires 1a–1d is reduced as follows:

$$dP_1/dt = 2[k_2P_2(1 - P_1) - k_{-2}P_1(1 - P_2)] - k_1P_1 + k_{-1}(1 - P_1)$$
(1a′)

$$dP_2/dt = \alpha[k_3P_3(1 - P_2) - k_{-3}P_2(1 - P_3)] \\ - k_2P_2(1 - P_1) + k_{-2}P_1(1 - P_2)$$
(1c′)

$$dP_3/dt = -k_3P_3(1 - P_2) + k_{-3}P_2(1 - P_3)$$
(1d′)

For $Au-[A_H(FeL)_2FeT]$:

$$dP_1/dt = 2[k_2P_2(1 - P_1) - k_{-2}P_1(1 - P_2)] - k_1P_1 + k_{-1}(1 - P_1)$$
(1a″)

$$dP_2/dt = 2[k_2P_3(1 - P_2) - k_{-3}P_2(1 - P_3)] \\ - k_2P_2(1 - P_1) + k_{-2}P_1(1 - P_2)$$
(1b″)

$$dP_3/dt = \alpha[k_3P_4(1 - P_3) - k_{-3}P_3(1 - P_4)] - k_2P_3(1 - P_2) \\ + k_{-2}P_2(1 - P_3)$$
(1c″)

$$dP_4/dt = -k_3P_4(1 - P_3) + k_{-3}P_3(1 - P_4)$$
(1d″)

For $Au-[A_H(FeL)_3FeT]$:

$$dP_1/dt = 2[k_2P_2(1 - P_1) - k_{-2}P_1(1 - P_2)] - k_1P_1 + k_{-1}(1 - P_1)$$
(1a‴)

$$dP_k/dt = 2[k_2P_{k+1}(1 - P_k) - k_{-2}P_k(1 - P_{k+1})] - k_2P_k(1 - P_{k-1}) \\ + k_{-2}P_{k-1}(1 - P_k) \quad (k = 2, \ 3)$$
(1b‴)

$$dP_4/dt = \alpha[k_3P_5(1 - P_4) - k_{-3}P_4(1 - P_5)] - k_2P_4(1 - P_3) \\ + k_{-2}P_3(1 - P_4)$$
(1c‴)

$$dP_5/dt = -k_3P_5(1 - P_4) + k_{-3}P_4(1 - P_5)$$
(1d‴)

For linear $Au-[A_H(FeL_L)_1FeT]$, the series of kinetic equations for linear wires 4a–4d is reduced as follows:

$$dP_1/dt = k_2P_2(1 - P_1) - k_{-2}P_1(1 - P_2) - k_1P_1 + k_{-1}(1 - P_1)$$
(4a′)

$$dP_2/dt = \alpha[k_3P_3(1 - P_2) - k_{-3}P_2(1 - P_3)] - k_2P_2(1 - P_1) \\ + k_{-2}P_1(1 - P_2)$$
(4c′)

$$dP_3/dt = -k_3P_3(1 - P_2) + k_{-3}P_2(1 - P_3)$$
(4d′)

In the case of $Au-[A_H(FeL_L)_2FeT]$, the following equations are employed:

$$dP_1/dt = k_2P_2(1 - P_1) - k_{-2}P_1(1 - P_2) - k_1P_1 + k_{-1}(1 - P_1)$$
(4a″)

$$dP_2/dt = k_2P_2(1 - P_3) - k_{-2}P_2(1 - P_3) - k_2P_2(1 - P_1) \\ + k_{-2}P_1(1 - P_2)$$
(4b″)

$$dP_3/dt = \alpha[k_3P_4(1 - P_3) - k_{-3}P_3(1 - P_4)] - k_2P_3(1 - P_2) \\ + k_{-2}P_2(1 - P_3)$$
(4c″)

$$dP_4/dt = -k_3P_4(1 - P_3) + k_{-3}P_3(1 - P_4)$$
(4d″)

where α is a scaling parameter for **T**. α is expressed as follows:
For branched $Au-[A_H(FeL)_nFeT]$:

$$\alpha = \frac{(2^{n+1} - 1)\Gamma_T}{2^n\Gamma_{Fe}}$$
(5)

For linear $Au-[A_H(FeL_L)_nFeT]$:

$$\alpha = \frac{n\Gamma_T}{\Gamma_{Fe}}$$
(6)

where Γ_T and Γ_{Fe} are the surface coverage of ferrocene and $Fe(tpy)_2$ units, respectively, which may be calculated from cyclic voltammetry (cf. Figure 3). Cyclic voltammetry also provides the surface coverage of the dendritic and linear wires, Γ in eq 2. The surface area of the electrode, A, was fixed at $0.264\ cm^2$.

The kinetic simulation was carried out according to the following procedures: [1] calculation of the electron population on the nth generation, [2] calculation of faradaic current i_F using eq 2, and [3] fitting the simulated redox current profile [i_{sim}, eq 3] with the experimental one (i_{exp}) by changing electron transfer rate constants k_l. As for the oxidation process, the initial occupations for all redox sites (P_n) were set at 1. The same is applicable for the reduction process, except that the initial population of terminal ferrocene was set at 0. Electric double layer charging current i_{DL} is represented as eq 7:

$$i_{DL} = \frac{|\Delta E|}{R_{sol}} \exp\left(-\frac{t}{R_{sol}C_{DL}}\right) \qquad (7)$$

where ΔE is the applied potential step (± 0.70 V), R_{sol} is the resistance of the electrolyte solution ($250-300\ \Omega$), C_{DL} is the capacity of electric double layer, and t is the time, respectively. C_{DL} may be estimated from a certain region of a cyclic voltammogram, where no faradaic current flows.[33]

Two conditions are used to simplify the simulation process. One is that condition $k_2 = k_{-2}$ is employed because of the self-electron-exchange process. The other is that k_2 and k_3 are fixed at constant values for oxidation and reduction, respectively, considering the same overpotential magnitude (i.e., +0.35 and −0.35 V).

■ ASSOCIATED CONTENT

Ⓢ Supporting Information

Preparation procedure for branched and linear $Fe(tpy)_2$ oligomer wires, surface coverages of Au-$[A_H(FeL)_{n+1}]$, a set of PSCA fitting for the remaining samples, parameters used in the PSCA fitting. This material is available free of charge via the Internet at http://pubs.acs.org.

■ AUTHOR INFORMATION

Corresponding Author
nisihara@chem.s.u-tokyo.ac.jp

Notes
The authors declare no competing financial interest.

■ REFERENCES

(1) Aviram, A.; Ratner, M. *Chem. Phys. Lett.* **1974**, *29*, 277.
(2) Carter, F. L. *Microelectron. Eng.* **1984**, *2*, 11.
(3) Carter, F. L. *Physica D* **1984**, *10*, 175.
(4) Carter, F. L. *Superlattices Microstruct.* **1986**, *2*, 113.
(5) Aviram, A. *J. Am. Chem. Soc.* **1988**, *110*, 5687.
(6) Lindsey, J. S.; Bocian, D. F. *Acc. Chem. Res.* **2011**, *44*, 638.
(7) de Ruiter, G.; van der Boom, M. E. *Acc. Chem. Res.* **2011**, *44*, 563.
(8) Uchida, K.; Yamanoi, Y.; Yonezawa, T.; Nishihara, H. *J. Am. Chem. Soc.* **2011**, *133*, 9239.
(9) Chidsey, C. E. D. *Science* **1991**, *251*, 919.
(10) Rowe, G. K.; Carter, M. T.; Richardson, J. N.; Murray, R. W. *Langmuir* **1995**, *11*, 1797.
(11) Luo, L.; Choi, S. H.; Frisbie, C. D. *Chem. Mater.* **2011**, *23*, 631.
(12) Wang, G.; Kim, T.-W.; Lee, T. *J. Mater. Chem.* **2011**, *21*, 18117.
(13) Mccreery, R. L.; Yan, H.; Bergren, A. J. *Phys. Chem. Chem. Phys.* **2013**, *15*, 1065.
(14) Vazquez, H.; Skouta, R.; Schneebeli, S.; Kamenetska, M.; Breslow, R.; Venkataraman, L.; Hybertsen, M. S. *Nat. Nanotechnol.* **2012**, *7*, 663.
(15) Inkpen, M. S.; Albrecht, T.; Long, N. J. *Organometallics* **2013**, *32*, 6053.
(16) Wanunu, M.; Vaskevich, A.; Shanzer, A.; Rubinstein, I. *J. Am. Chem. Soc.* **2006**, *128*, 8341.
(17) Choudhury, J.; Kaminker, R.; Motiei, L.; de Ruiter, G.; Morozov, M.; Lupo, F.; Gulino, A.; van der Boom, M. E. *J. Am. Chem. Soc.* **2010**, *132*, 9295.
(18) Sakamoto, R.; Katagiri, S.; Maeda, H.; Nishihara, H. *Coord. Chem. Rev.* **2013**, *257*, 1493.
(19) Maeda, H.; Sakamoto, R.; Nishihara, H. *Polymer* **2013**, *54*, 4383.
(20) Nishimori, Y.; Kanaizuka, K.; Murata, M.; Nishihara, H. *Chem.—Asian J.* **2007**, *2*, 367.
(21) Maeda, H.; Sakamoto, R.; Nishimori, Y.; Sendo, J.; Toshimitsu, F.; Yamanoi, Y.; Nishihara, H. *Chem. Commun.* **2011**, *47*, 8644.
(22) Nishimori, Y.; Kanaizuka, K.; Kurita, T.; Nagatsu, T.; Segawa, Y.; Toshimitsu, F.; Muratsugu, S.; Utsuno, M.; Kume, S.; Murata, M.; Nishihara, H. *Chem.—Asian J.* **2009**, *4*, 1361.
(23) Kurita, T.; Nishimori, Y.; Toishimitsu, F.; Muratsugu, S.; Kume, S.; Nishihara, H. *J. Am. Chem. Soc.* **2010**, *132*, 4524.
(24) Sakamoto, R.; Ohirabaru, Y.; Matsuoka, R.; Maeda, H.; Katagiri, S.; Nishihara, H. *Chem. Commun.* **2013**, *49*, 7108.
(25) Katagiri, S.; Sakamoro, R.; Maeda, H.; Nishimori, Y.; Kurita, T.; Nishihara, H. *Chem.—Eur. J.* **2013**, *19*, 5088.
(26) Denisevich, P.; Willman, K. W.; Murray, R. W. *J. Am. Chem. Soc.* **1981**, *103*, 4727.
(27) de Ruiter, G.; Lahav, M.; Keisar, H.; van der Boom, M. E. *Angew. Chem., Int. Ed.* **2013**, *52*, 704.
(28) de Ruiter, G.; Lahav, M.; Evmenenko, G.; Dutta, P.; Cristaldi, D. A.; Gulino, A.; van der Boom, M. E. *J. Am. Chem. Soc.* **2013**, *135*, 16533.
(29) Sek, S.; Palys, B.; Bilewicz, R. *J. Phys. Chem. B* **2002**, *106*, 5907.
(30) Ju, H.; Leech, D. *Langmuir* **1998**, *14*, 300.
(31) Siemeling, U.; Vor der Brüggen, J.; Vorfeld, U.; Neumann, B.; Stammler, A.; Stammler, H.-G.; Brockhinke, A.; Plessow, R.; Zanello, P.; Laschi, F.; de Biani, F. F.; Fontani, M.; Steeken, S.; Stapper, M.; Gurzadyan, G. *Chem.—Eur. J.* **2003**, *9*, 2819.
(32) Cavazzni, M.; Quici, S.; Scalera, C.; Puntoriero, F.; La Ganda, G.; Campagna, S. *Inorg. Chem.* **2009**, *48*, 8578.
(33) Eckermann, A. L.; Feld, D. J.; Shaw, J. A.; Meade, T. J. *Coord. Chem. Rev.* **2010**, *254*, 1769.